Atomic Force Microscopy Studies of Functional and Dysfunctional Pulmonary Surfactant Films. I. Micro- and Nanostructures of Functional Pulmonary Surfactant Films and the Effect of SP-A

Yi Y. Zuo,*†‡ Eleonora Keating,* Lin Zhao,‡ Seyed M. Tadayyon,* Ruud A. W. Veldhuizen,§ Nils O. Petersen,*†¶ and Fred Possmayer†‡

*Department of Chemistry, †Department of Biochemistry, ‡Department of Obstetrics and Gynaecology, §Departments of Physiology and Pharmacology and Medicine, University of Western Ontario, London, Ontario, Canada; and ¶National Institute for Nanotechnology, National Research Council Canada, Edmonton, Alberta, Canada

ABSTRACT Monolayers of a functional pulmonary surfactant (PS) can reach very low surface tensions well below their equilibrium value. The mechanism by which PS monolayers reach such low surface tensions and maintain film stability remains unknown. As shown previously by fluorescence microscopy, phospholipid phase transition and separation seem to be important for the normal biophysical properties of PS. This work studied phospholipid phase transitions and separations in monolayers of bovine lipid extract surfactant using atomic force microscopy. Atomic force microscopy showed phospholipid phase separation on film compression and a monolayer-to-multilayer transition at surface pressure 40–50 mN/m. The tilted-condensed phase consisted of domains not only on the micrometer scale, as detected previously by fluorescence microscopy, but also on the nanometer scale, which is below the resolution limits of conventional optical methods. The nanodomains were embedded uniformly within the liquid-expanded phase. On compression, the microdomains broke up into nanodomains, thereby appearing to contribute to tilted-condensed and liquid-expanded phase remixing. Addition of surfactant protein A altered primarily the nanodomains and promoted the formation of multilayers. We conclude that the nanodomains play a predominant role in affecting the biophysical properties of PS monolayers and the monolayer-to-multilayer transition.

INTRODUCTION

Pulmonary surfactant (PS) is a complicated mixture of ~80 wt% phospholipids (PL), 5–10% neutral lipids (primarily cholesterol), and 5–10% proteins (1). It is secreted by pulmonary type II epithelial cells and plays a crucial role in maintaining normal respiratory mechanics. At least three biophysical properties of PS are essential for normal respiratory physiology, especially in the neonatal period. They are rapid adsorption, very low surface tension on film compression, and effective film replenishment on film expansion (1). Although still controversial at the mechanistic level, the current consensus attributes the rapid adsorption and the effective readsorption and reinsertion of PL vesicles after film collapse to the presence of hydrophobic surfactant proteins, i.e., SP-B and SP-C (2–5). Compared to adsorption, however, how surfactant films reach low surface tensions is not nearly as clear (6).

In situ measurements suggested that PS films can lower the alveolar surface tension to near-zero values at end expiration and are able to maintain these low values for prolonged periods (7). In other words, functional PS films should be capable of increasing the surface pressure (π) to a value close to 70 mN/m at 37°C. This π is substantially higher than the equilibrium spreading pressure (π_e) of PL vesicles, i.e., ~45–50 mN/m (1). Hence, the surfactant film must be in a metastable state. Traditional tensiometric studies using Langmuir-Wilhelmy balances suggested that only highly rigid insoluble molecules allow the formation of highly ordered, tightly packed, solid-like monolayers in tilted-condensed (TC) phases, thus being capable of sustaining π higher than π_e without monolayer collapse (8). Fully hydrated dipalmitoyl phosphatidylcholine (DPPC) bilayers have a gel to liquid crystal phase transition temperature near 41°C (1). Hence, DPPC is traditionally taken as being the only significant component of PS capable of reaching high π at the physiological temperature of 37°C. However, the DPPC content in mammalian PS is generally no more than 40% (9,10). This apparent discrepancy led to the classical ''squeeze-out'' model that predicts that the less stable fluid non-DPPC components are gradually squeezed out of the interfacial monolayer during film compression (11–13). This selective squeeze-out process would result in a TC monolayer highly enriched in DPPC that is responsible for reaching very low surface tensions (11–13).

During the last decade, a variety of microscopic and spectroscopic techniques have been introduced to PS studies. Application of these surface analysis techniques facilitates direct imaging of surfactant films in different perspectives, such as domain formation shown by fluorescence microscopy (FM) (14–16) and Brewster angle microscopy (BAM) (17–19), surface topography studied by atomic force microscopy (AFM) (20–22), and localized chemical compositions examined by

Submitted September 21, 2007, and accepted for publication December 21, 2007.

Address reprint requests to Fred Possmayer, Depts. of Obstetrics/Gynaecology and Biochemistry, The University of Western Ontario Schulich School of Medicine and Dentistry, Dental Sciences Building 5009, London, Ontario, Canada N6A 5C1. Tel.: 519-661-2111, ext. 80972; Fax: 519-661-3175; E-mail: fpossmay@uwo.ca.

Editor: Thomas Schmidt.

0006-3495/08/05/3549/16 $2.00

doi: 10.1529/biophysj.107.122648

time-of-flight secondary ion mass spectrometry (ToF-SIMS) (23–25). These film imaging/analysis techniques have provided valuable information that complements the traditional tensiometry techniques. One of the most important findings from these imaging techniques is the invalidation of the classical squeeze-out model. As shown by AFM, PS monolayers at π 40 mN/m at 25°C clearly showed coexisting TC and liquid-expanded (LE) domains (26). In contrast, pure DPPC monolayers at room temperature showed LE–TC phase transition/coexistence only from 9 to 13 mN/m (27). At higher π pure DPPC monolayers showed a homogeneous TC phase until irreversible collapse occurred at ~70 mN/m (26, 27). The results from recent FM studies further showed that TC–LE phase coexistence of the PL fraction of PS at room temperature persisted even at π approaching 70 mN/m (19). Despite the apparent deviations of the experimental conditions from the physiological environment (such as temperature, humidity, and surfactant composition), these findings on PL phase separation all argued against the classical interpretation that PS films reach low surface tensions by forming homogeneous TC DPPC monolayers. The TC domains are enriched in DPPC (18) and hence intrinsically stable at high π. However, how the LE domains, which account for most of the surface area (19), persist at high π remains unknown.

Previous studies of PL phase transitions and separations mainly relied on ''model'' surfactants consisting of simple PL/hydrophobic protein mixtures, or organic extracted surfactants. Surfactant protein A (SP-A) is absent from all of these hydrophobic preparations. SP-A is the most abundant surfactant protein by mass accounting for ~5% of PS (28). It is a hydrophilic glycoprotein with a monomeric molecular mass of 26–38 kDa (29). The native form of SP-A, as isolated from the alveolar space, forms octadecamers in which SP-A chains are organized in trimers through their collagen-like regions (30). SP-A is a member of the Ca^{2+}-dependent carbohydrate-binding collectin family (29). Although lacking intrinsic surface activity, SP-A promotes the surface activity of PS in cooperation with the hydrophobic surfactant protein SP-B and calcium (31). In vitro experiments show that SP-A is necessary for the formation of tubular myelin (32) and is important for maintaining large surfactant aggregates (33), i.e., the highly surface active proportion of PS. A small amount of SP-A can significantly enhance adsorption of lipid extract surfactants, thereby increasing their surface activity at reduced PL concentrations (34,35).

We studied the film conformation of a clinical surfactant, bovine lipid extract surfactant (BLES), with and without SP-A using AFM. AFM has been proven to be an ideal imaging technique for studying PL membranes (36). It is superior to the conventional optical microscopic methods such as FM in providing a higher spatial resolution and eliminating the need of fluorescence probes (37). In addition, AFM can show not only 2D, but also 3D topographic structures and hence is capable of studying both monomolecular and supramolecular conformations of PS films (20,21). In this study, AFM clearly showed PL phase separation in BLES monolayers on film compression and a monolayer-to-multilayer transition occurring at π 40–50 mN/m. The condensed phase in BLES monolayers consisted of domains not only on the micrometer scale, as detected previously by FM, but also on the nanometer scale, which is below the resolution limits of conventional optical methods. It was found that the nanodomains generally account for a significantly larger surface area than the microdomains, especially just before the onset of the monolayer-to-multilayer transition. This indicates that the nanodomains may play a predominant role in affecting the biophysical properties of functional PS films. Addition of SP-A to BLES altered primarily the nanodomains and promoted the formation of multilayers. To the best of our knowledge, this is the first detailed study that shows the π-dependent evolution of both micro- and nanostructures in a natural PS. These results may lead to a better understanding of the biophysical properties of PS at a molecular level.

MATERIALS AND METHODS

Materials

BLES (BLES Biochemicals Inc., London, ON, Canada) is a commercially available, clinical preparation. BLES is prepared by organic extraction of lung foam obtained by bronchopulmonary lavage. Acetone extraction is carried out to remove cholesterol (38). BLES contains all of the PL in natural surfactant and the hydrophobic surfactant proteins, SP-B and SP-C. The proteins account for ~2 wt% as determined by amino acid analysis (39). The PL consists of ~80% phosphatidylcholine (PC), 14% phosphatidylglycerol (PG), and minor amounts of other classes (38). DPPC (16:0, 16:0 PC) and palmitoyl-oleoyl PC (POPC) (16:0, 18:1 PC) are the most abundant PC species, which account for 37% and 21% of the PC class, respectively (40). Palmitoyl-oleoyl PG (POPG) (16:0, 18:1 PG) and dipalmitoyl PG (DPPG) (16:0, 16:0 PG) are the most abundant PG species, accounting for 44% and 21% of the PG class, respectively (40). Detailed mass spectroscopic analysis of the remaining PL species in BLES can be found elsewhere (38,40).

BLES was stored frozen in physiological saline, 1.5 mM $CaCl_2$, with an initial concentration of 27 mg/mL. BLES samples were prepared in two different ways for film spreading. For spreading from aqueous media, BLES was diluted to 5 mg/mL using a saline buffer of 0.9% NaCl, 1.5 mM $CaCl_2$, and 2.5 mM HEPES at pH 7.0. For spreading from organic solvent, BLES was first extracted by chloroform:methanol using a method modified from Bligh and Dyer (41). The chloroform:methanol extract was dried under a nitrogen stream and redissolved in chloroform to a final concentration of 1 mg/mL. The chloroform extracted BLES was stored at −20°C until use. All solvents used were HPLC grade. The water used was Milli-Q ultrapure water (Millipore., Billerica, MA), which has a resistivity higher than 18 MΩ/cm at room temperature.

Human SP-A was isolated from the whole lung lavage of an alveolar proteinosis patient using butanol extraction with further purification as described elsewhere (42,43). The biophysical properties of this purified SP-A were found to be similar to bovine SP-A when added to BLES (43). The concentration of SP-A was determined by a modified method of Lowry et al. (39,44). SP-A was stored at −20°C in 5 mM Tris-HCl until use. SP-A was added to BLES at 2.5% relative to the weight of PL in BLES. In some experiments, 5 mM EDTA was first mixed with BLES to deplete calcium ions before adding SP-A.

Langmuir-Wilhelmy balance

The spreading, compressing and Langmuir-Blodgett (LB) transferring of surfactant films was conducted in a Langmuir-Wilhelmy balance (LWB)

(μ-Trough, Kibron, Helsinki, Finland) at room temperature (24 ± 1°C). The balance is equipped with a continuous Teflon ribbon to minimize film leakage. The trough contains a ~90 mL subphase and has an operational surface area of ~125 cm^2.

Film spreading

All films were prepared by spreading samples on ultrapure water. Films were spread by depositing tiny droplets of samples uniformly throughout the air–water interface using a 10 μL microsyringe. BLES films were spread from either 15 μL chloroform-extracted BLES at 1 mg/mL or 15–20 μL aqueous suspended BLES at 5 mg/mL. Both methods increased π identically to 1–3 mN/m. When LB transfer at a high π (i.e., 50 mN/m) was required, larger amounts of samples were spread to increase the initial π to ~30 mN/m. Strictly speaking, when films were spread from an aqueous medium both spreading and adsorption may occur at the interface. Some PL vesicles may spread immediately at the interface when they touch the interface, whereas others may first penetrate the interface and then adsorb back with time. In addition, some vesicles diffuse into the subphase. As a result, it usually requires a larger amount of samples for spreading from aqueous media than from organic solvents to produce a similar π. In this study, we do not attempt to distinguish these two film formation processes when films are prepared from aqueous media. For the preparation of BLES films with SP-A, the films were spread from aqueous mixtures of 5 mg/mL BLES with 2.5% SP-A. Spreading 7–10 μL BLES with SP-A resulted in a π of 5–10 mN/m.

After spreading, all films were left undisturbed for 10 min to allow equilibrium and evaporation of solvent (if used). During film spreading and the following 10-min period, surface pressure–time (π–t) isotherms were recorded.

Film compression

Spread films were compressed at a rate of 30 mm^2/s, namely 0.24% initial area per second, unless otherwise indicated. During compression, surface pressure–area (π–A) isotherms were recorded. Here, the relative area (%), normalized to the initial surface area before compression, rather than the absolute molecular area was used. This is due to the difficulty of controlling the exact amount of surfactant molecules at the air–water interface (thus the accurate molecular area) when the films were spread from aqueous media. The use of relative area also facilitates the comparison of π–A isotherms of surfactant films spread from different amounts of samples.

Film transfer

For AFM imaging, surfactant films at the air–water interface were transferred to the surface of freshly cleaved mica using the LB technique. Surfactant films at controlled constant π were deposited onto the mica surface by elevating the previously submerged mica vertically through the air–water interface at a rate of 2 mm/min. Deposited films were scanned by AFM within 2 hr of deposition. Aging of LB films in air over this time period is considered to have negligible effects on film structure (45).

Atomic force microscopy

Topographical AFM images were obtained using a Nanoscope III scanning force multimode microscope (Digital Instruments, Santa Barbara, CA). Samples were scanned with a J type scanner using contact mode in air. A silicon nitride cantilever with a spring constant of 0.12 N/m was used. Analysis of the AFM images was carried out using the Nanoscope III software (version 5.12r3).

Image analysis

Scion Image (Scion, Frederick, MD) was used to quantify the areas and sizes of the condensed domains in the AFM images. The areas (A) and perimeters (P) of the domains were the output of image analysis. The sizes, i.e., the equivalent diameters, of the domains were calculated using their hydraulic diameters, $d_h = 4A/P$. Each quantification result was averaged from multiple frames of different samples at different resolutions.

RESULTS

BLES films

Fig. 1 shows compression isotherms of BLES films and the isobaric curves at which the films were LB transferred onto mica. As shown in Fig. 1, films spread from 15 μL 1 mg/mL BLES in chloroform and from 20 μL 5 mg/mL BLES in aqueous suspension yield nearly identical compression isotherms. They both increased π to 1–3 mN/m before compression. As the films are compressed, the π first increases

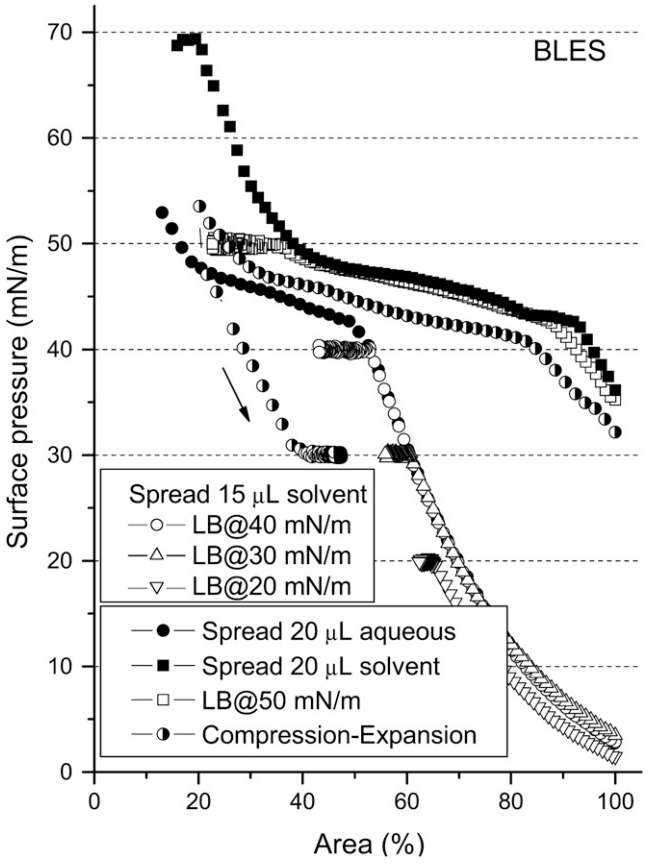

FIGURE 1 Compression, isobaric and expansion isotherms of BLES films. BLES films were spread on distilled water from either 1 mg/mL chloroform solution or 5 mg/mL aqueous suspension at room temperature. The films were compressed at a rate of 30 mm^2/s and LB transferred at 20, 30, 40, and 50 mN/m. Films spreading from 15 μL chloroform samples and from 20 μL aqueous samples yielded nearly identical compression isotherms. To transfer a film at 50 mN/m, 20 μL chloroform samples were spread, which increased the initial π to >30 mN/m. A plateau was found at 40–50 mN/m. After passing the plateau, the π quickly increased up to ~70 mN/m where the film collapsed. A film was expanded (as indicated by an arrow) after being compressed to a π higher than 50 mN/m. The expanded film was LB transferred at 30 mN/m to mica.

rapidly, then reaches a plateau at 40–50 mN/m, and increases steeply again after passing the plateau. Limited by mechanical design, the LWB used in this study can only reach a minimum surface area of 15–20%, which restricts the maximum π. To reach a higher π, 20 μL BLES in chloroform was spread, which increased the initial π to >30 mN/m. This high initial π, however, does not vary the location of the plateau in the compression isotherms, although it spans a longer distance of compression. After passing the plateau, the π increased steeply up to 70 mN/m where the film collapsed.

Characteristic AFM images of BLES films obtained at increasing π are shown in Fig. 2, *A–D*. The brightness in these images is proportional to the height. Phase separation is clear at 20 mN/m where kidney-shaped or oval TC domains with a microscale size (~2 μm) appear in the monolayer (Fig. 2 *A*). The PL molecules in these TC domains are in a closely-packed gel phase where their acyl chains tilt at smaller angles than the PL molecules in the surrounding LE domains (27). The height difference between the TC and LE domains detected by AFM is in the range of 0.6–1.0 nm (see the cross-sectional profiles shown in Fig. 2). This is in a good agreement with the thickness difference of stacked PL bilayers in gel and liquid crystalline phases (46). It is also consistent with the domain topography found previously in simple PL (26) and BLES (24) monolayers.

Increasing π from 20 to 30 mN/m (Fig. 2 *B*) increased the number of microscale TC domains, called ''microdomains'' hereafter, and additionally induced the formation of nanoscale TC domains, i.e., the ''nanodomains''. The nanodomains are not detectable at 20 mN/m. However, at 30 mN/m, the

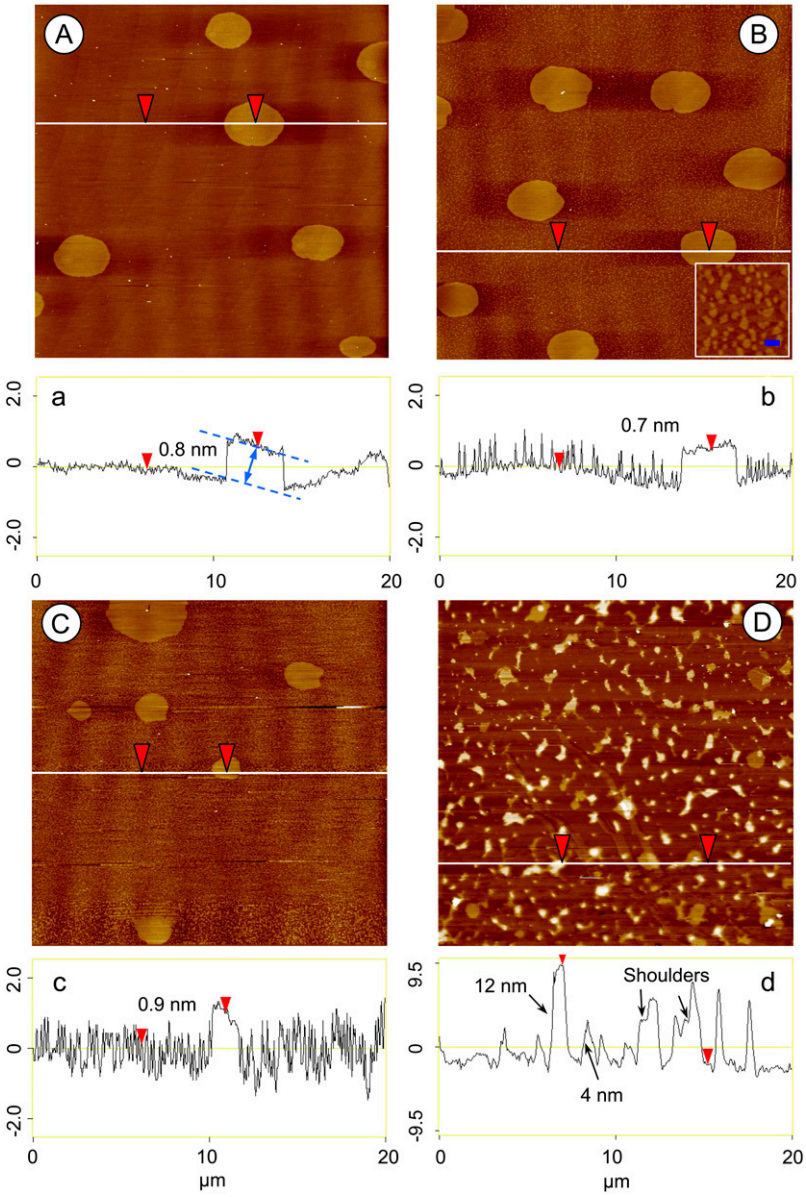

FIGURE 2 Characteristic AFM topographic images of BLES films at increasing π. The scan area is 20 × 20 μm. (*A*) 20 mN/m; (*B*) 30 mN/m; (*C*) 40 mN/m; (*D*) 50 mN/m. (*a–d*) Height variation along the scanning line drawn in the corresponding topographical images. The measured distance between the arrowheads is indicated in the cross-sectional profile. It shows the approximate heights of the kidney-shaped TC domains relative to the surrounding LE domains. The inset in (*B*) shows an enlargement of nanodomains embedded in the LE phase. The bar shown in the inset represents 200 nm. A transition from monolayer to multilayers is clear at 50 mN/m, where the vertical scale is fourfold that of the monolayers (20 nm vs. 5 nm) as shown in the cross-sectional profiles. Some multilayers show a feature of stacked bilayers, as indicated by the shoulders in *d*.

nanodomains are clearly shown by the cross-sectional profile. Fig. 2 *b* shows significant fluctuations in height along the scanning line indicated in Fig. 2 *B*. These fluctuations, i.e., nanodomains, are relatively homogeneous topographically and have approximately the same height as the microdomains, thus indicating that the nanodomains may consist of similar materials in a similar phase as the microdomains. The inset in Fig. 2 *B* shows an enlargement of the nanodomains. These nanodomains are uniformly embedded within the LE domains and have an average size of ~60 nm. The total area of these nanodomains approximately doubles the area of the microdomains (see Fig. 3 for detailed quantification results). Together with the increasing number of microdomains, the presence of these nanodomains significantly increases the proportion of the TC phase in the monolayer (Fig. 3 *A*).

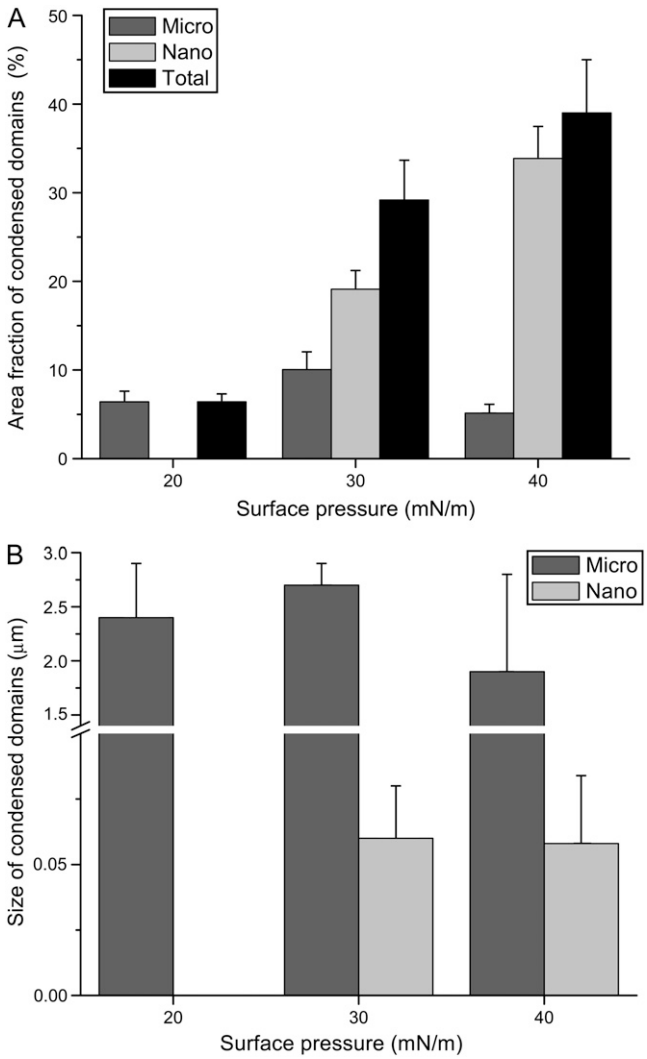

FIGURE 3 Quantification results of the development of microscale, nanoscale, and total TC domains in BLES monolayers on compression. (*A*) Surface areas covered by the TC domains. (*B*) Size, i.e., equivalent diameter, of micro- and nanodomains. These results were quantified from multiple images of different samples and images at different resolutions.

Increasing π from 30 to 40 mN/m (Fig. 2 *C*) destabilized the microdomains but promoted the formation of more nanodomains. Compared to lower π, the number and average size of the microdomains at 40 mN/m decreased. In contrast, the number of nanodomains (with a similar size to those at 30 mN/m) significantly increased, as indicated by the intensive variation shown in the cross-sectional profile (Fig. 2 *c*). Owing to the increased number of the nanodomains, the total area fraction of the film covered by the TC phase increases from ~30% to ~40% despite the decrease of the microdomains (Fig. 3 *A*).

A dramatic change in film conformation was found when π was further increased to 50 mN/m (Fig. 2 *D*). At this π, the film showed protrusions that are significantly higher than a monolayer. This indicates a transition of the original 2D monolayer into 3D structures by partial collapse of the monolayer at 40–50 mN/m. Such 2D–3D transitions in molecular arrangements coincided with the plateau in the compression isotherms (Fig. 1). Due to the multilayered nature of the film at 50 mN/m, the concepts of TC and LE phases, defined for monolayers, are no longer directly applicable. Some researchers consider these 3D protrusions as a separated phase, called ''collapsed phase'' (47). To distinguish the reversible (as will be shown later), partial collapse at this π range from the ultimate, irreversible collapse occurring at ~70 mN/m, we simply refer to these protrusions as ''multilayers''. These multilayers cover ~15% of the projected area of the film. They show irregular fractal shapes with an average size of ~0.3 μm. The height of these protrusions ranges from ~4 to ~12 nm, corresponding to 1–3 stacks of PL bilayers (46). A close scrutiny of the topographical profile of these protrusions (Fig. 2 *d*) found two different morphologies: isolated protrusions and layered protrusions with shoulders (as indicated by the arrows in Fig. 2 *d*).

Reversibility of the monolayer-to-multilayer transition was studied where the BLES films were first compressed beyond 50 mN/m and then expanded back to lower π (see Fig. 1 for a compression–expansion isotherm 4). The AFM image of such an expanded film at 30 mN/m is shown in Fig. 4 *A*. The film shows a monolayer structure with micro- and nanodomains similar to, but not identical to, the domains present at the same π during compression (Fig. 2 *B*). This indicates that the multilayer structures formed during compression are able to reinsert and respread back into the interfacial monolayer during expansion.

Previous studies using FM found similar domain formation in adsorbed PS films compared to films compressed to the same π (16). Conventional AFM is not capable of studying surfactant films in situ at the air–water interface. LB transfer of the film requires the subphase in which the mica surface is submerged to be relatively clean. Hence, we could not directly study films adsorbed from PL vesicles using AFM. Instead, we studied BLES films at controlled π by accumulating sufficient surface active material at the air–water interface. Fig. 4 *B* shows an AFM image of a BLES film spread to

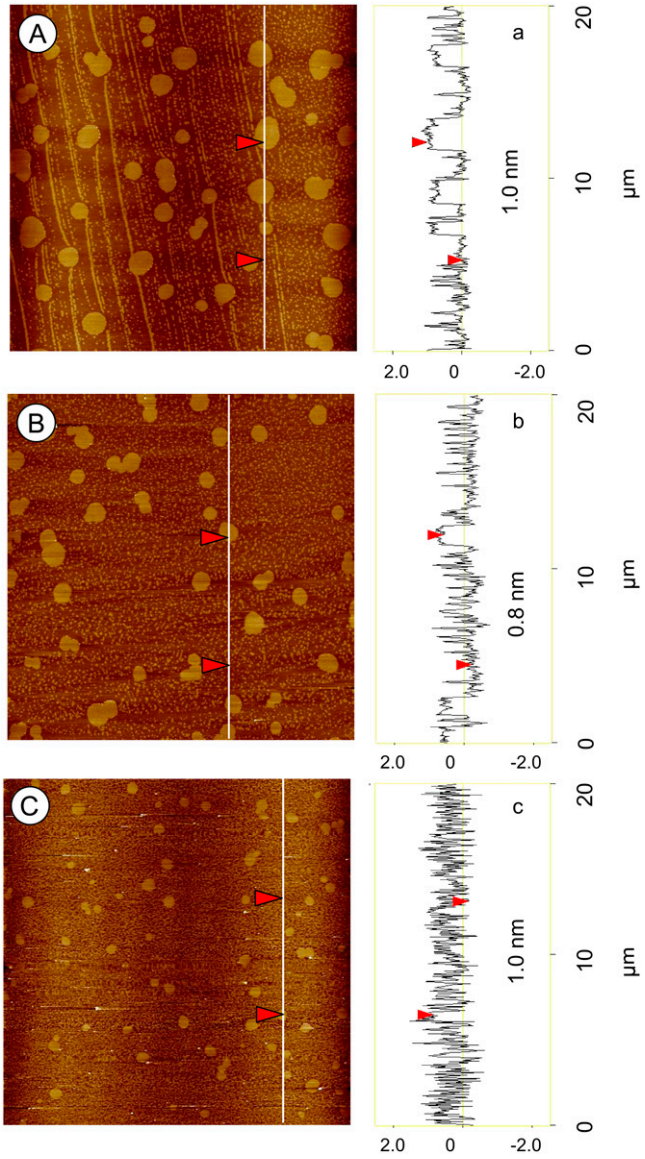

FIGURE 4 Characteristic AFM images of BLES monolayers at 30 mN/m under different conditions. The scan area is 20 × 20 μm. (*A*) A BLES film was first compressed to a π higher than 50 mN/m and then expanded to 30 mN/m, as indicated by the compression-expansion isotherm shown in Fig. 1. The basis of the streaks in this image, which have sometimes been observed in other AFM images, remains unknown. (*B*) A BLES film was spread at the air–water interface to a π of 30 ± 1 mN/m. The entire spreading process was completed within 10 s. (*C*) A BLES film was compressed rapidly to 30 mN/m. The rate of compression was 4.5 cm^2/s, 15 times faster than the compression rate used to obtain Fig. 2.

30 ± 1 mN/m using 20 μL samples. The spreading process was completed within ~10 s. Both micro- and nanodomains are shown clearly. Compared to the BLES films compressed to 30 mN/m (Fig. 2 *B*), there are more microdomains but with smaller sizes. This variation in the morphology of the microdomains is consistent with that reported by Nag et al. for adsorbed porcine surfactant films (16).

The rate of film compression used to yield the AFM images shown in Fig. 2 is only 0.24%/s, much slower than the compression rate estimated in the lungs, i.e., ~4%/s (47). To examine the effect of compression rate on the film topography, a BLES film was compressed at 3.6%/s, the maximum compression rate that can be operated in our LWB. Fig. 4 *C* shows an AFM image obtained at 30 mN/m on the fast compression. Compared to the BLES film at the same π but produced by slow compression (Fig. 2 *B*), the rapid compression yields a film with significantly more domains but with smaller sizes. The two main domain populations found in the film are both in the submicron size, ~0.7 and 0.15 μm, respectively.

BLES with SP-A

Fig. 5 shows the compression isotherms of BLES films with 2.5% SP-A (relative to the PL in BLES) spread from aqueous suspensions. Compression isotherms of films spread from

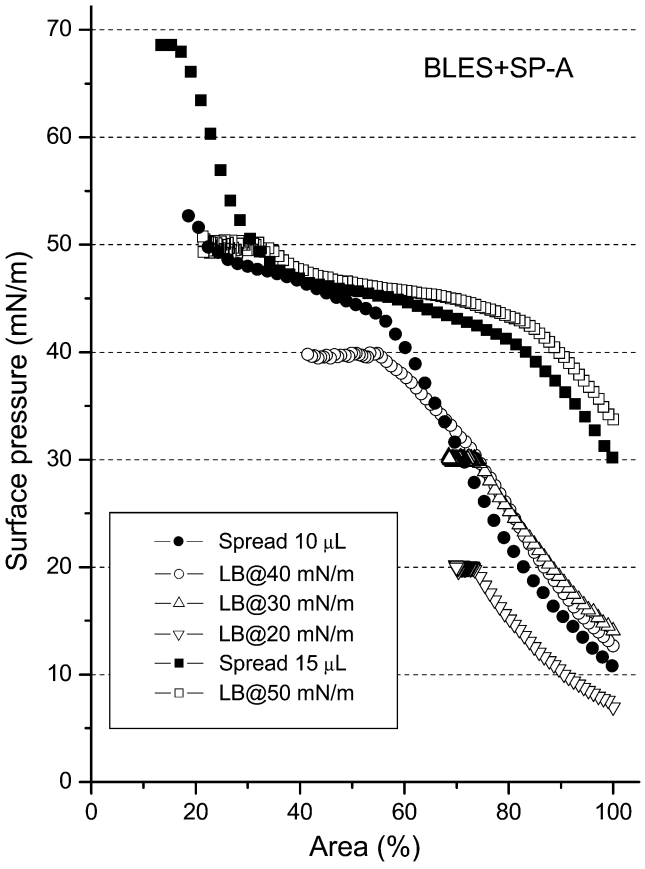

FIGURE 5 Compression and isobaric isotherms of BLES films with SP-A. The films were spread from an aqueous suspension of 5 mg/mL BLES with 2.5 wt% (relative to PL in BLES) human SP-A. The subphase and rate of compression are the same as those used in Fig. 1. The volume for spreading was 10 μL, unless a high π for LB transfer was required. To deposit a film at 50 mN/m, 15 μL samples were spread, which increased the initial π to >30 mN/m.

10 μL samples generally showed good reproducibility. To transfer films at 50 mN/m, 15 μL samples were spread, which increased the initial π to >30 mN/m. In comparison with the isotherms obtained without SP-A (Fig. 1), only half the amount of BLES was needed to increase π to 3–5 mN/m, indicating that SP-A facilitates adsorption and spreading of BLES vesicles. Similar to BLES films without SP-A, a plateau appears at 40–50 mN/m, which is independent of the initial amount of spreading.

Fig. 6, *A–D* shows characteristic AFM images of BLES films with SP-A. The evolution of microdomains as a function of π is found to be similar to that in BLES films without SP-A: the area of microdomains first increases when π is increased from 20 to 30 mN/m but decreases at 40 mN/m (see Fig. 8 for detailed quantification results). In contrast to pure BLES films, the addition of SP-A gives rise to two distinct features as follows.

First, SP-A promotes the formation of nanodomains. Nanodomains appear at 20 mN/m (Fig. 6A) where they are absent without SP-A. The nanodomains are shown clearly in Fig. 7 *A* that shows enlargement of the region indicated by the square box in Fig. 6 *A*. These nanodomains have a size of ~80 nm, slightly larger than those observed in pure BLES films at 30 mN/m. At 40 mN/m, i.e., immediately before the monolayer-to-multilayer transition, the area ratio of nanodomains to microdomains rose to ~18:1, significantly larger than the ratio of ~7:1 found in BLES films without SP-A. However, it should be noted that the total area of the TC domains is relatively unchanged with the addition of SP-A (Figs. 3 and 8).

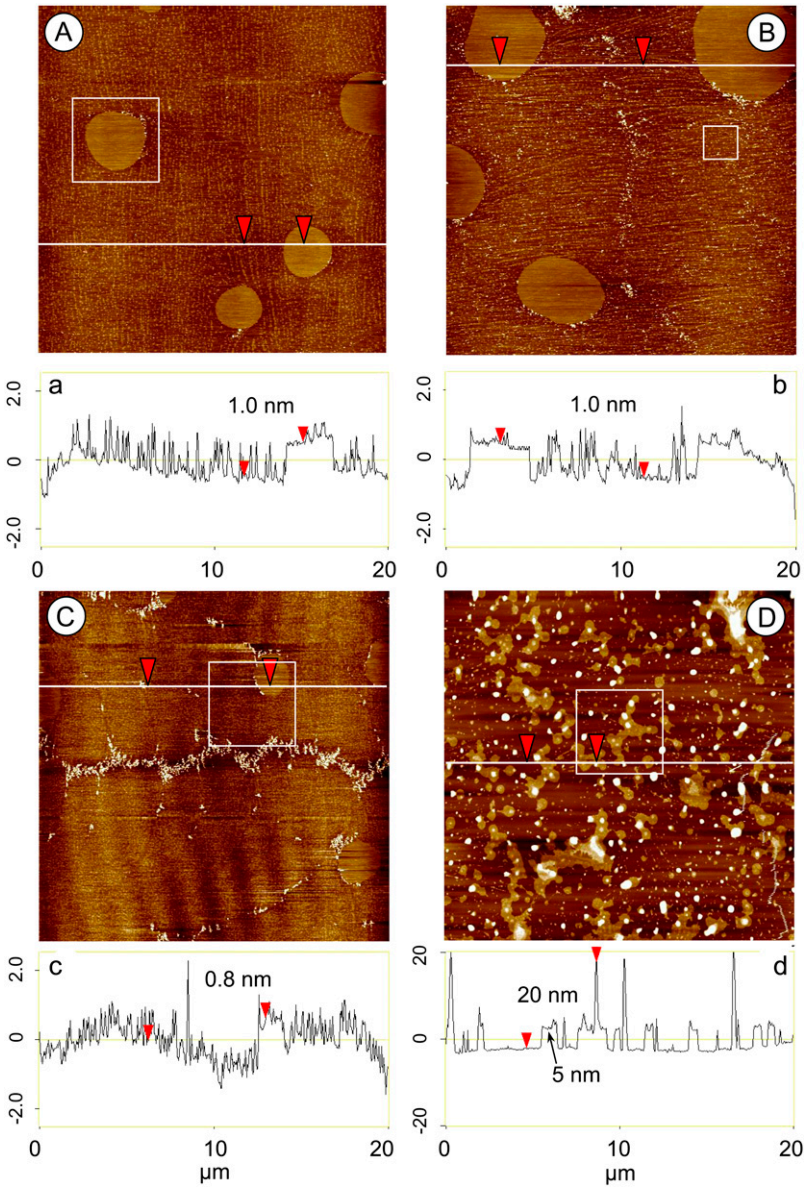

FIGURE 6 Characteristic AFM topographic images of BLES films with SP-A at increasing π. The scan area is 20 × 20 μm. (*A*) 20 mN/m; (*B*) 30 mN/m; (*C*) 40 mN/m; (*D*) 50 mN/m. (*a–d*) Height variation along the scanning line drawn in the corresponding topographical images. The measured distance between the arrowheads is indicated in the cross-sectional profile. A transition from monolayer to multilayer is clear at 50 mN/m, where the vertical scale is eightfold that of the monolayers (40 nm vs. 5 nm) as shown in the cross-sectional profiles. The regions indicated by the squares in the AFM images are magnified in Fig. 7.

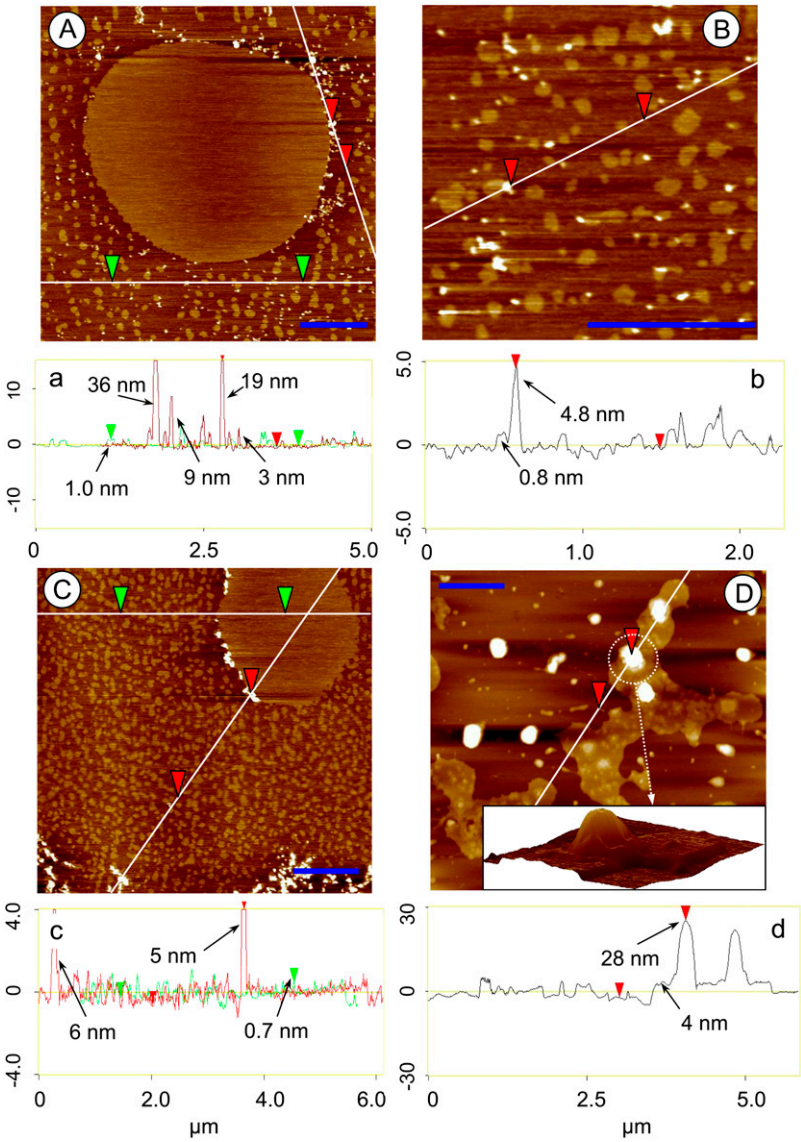

FIGURE 7 Detailed AFM images of BLES films with SP-A, as indicated by the square boxes in Fig. 6. The bar shown in these images represents 1 μm. (*A*) 20 mN/m. The image shows clearly the nanodomains that are undetectable in pure BLES films at the same π. It also shows bright spots associated with the microscale TC–LE domain boundaries. Height (measured distance in the cross-sectional profile) of these spots varies proportional to their size (horizontal distance in the cross-sectional profile). (*B*) 30 mN/m. The image shows that some of these bright spots are associated with the nanodomains embedded in the LE domains. (*C*) 40 mN/m. The image shows that except for a few associated with the microscale TC–LE domain boundaries in discrete patches, the majority of spots are self-associated into networks and are excluded from the LE phase. (*D*) 50 mN/m. The inset shows clearly a structure of stacked bilayers. The maximum height of the multilayers is greater than the multilayers in pure BLES films at the same π.

Second, with the addition of SP-A, many very bright spots, well beyond the height of a PL monolayer, appear. The size and height of these bright spots vary but seem to be correlated: the larger the spots the higher they are. As shown in Fig. 7 *a*, the size of these spots ranged from ~20 nm to ~100 nm, with their heights varying from ~3 nm to ~40 nm. It was also found that these spots are preferentially associated with the TC–LE domain boundaries, although a lesser portion is distributed in the LE phase. At 30 mN/m, more bright spots appear and are concentrated at the domain boundaries (Fig. 6 *B*). A high resolution image (Fig. 7 *B*) showed that some of the spots distributed in the LE phase may also be associated with the nanoscale TC domains at the domain boundaries. At 40 mN/m, although there are still a few spots attached to the microscale TC–LE domain boundaries, the majority of them coalesced with each other and formed loose networks (Fig. 6 *C*). As detailed in Fig. 7 *C*, these networks are associated with neither the nanoscale TC domains nor the LE phase, thus indicating that they may have been excluded from the monolayer.

Because they are absent from BLES films without SP-A, these bright spots are expected to be SP-A octadecamers or their aggregates. The dimensions of these individual bright spots, measured by AFM, are consistent with the size of SP-A octadecamers previous reported by Voss et al. (30). They found that the six collagen triple helices of SP-A molecules form a bundle of ~10 nm in length and 4.5 nm in diameter (30). AFM shows that the height of these aggregates is proportional to their size (Fig. 7 *a*), reflecting the nature of the self-association. Ruano et al. (48) found that self-association of SP-A octadecamers requires micromolar concentrations of calcium in the presence of physiological saline at neutral pH and room temperature. To verify our hypothesis, AFM images of BLES films with SP-A and 5 mM EDTA were obtained at

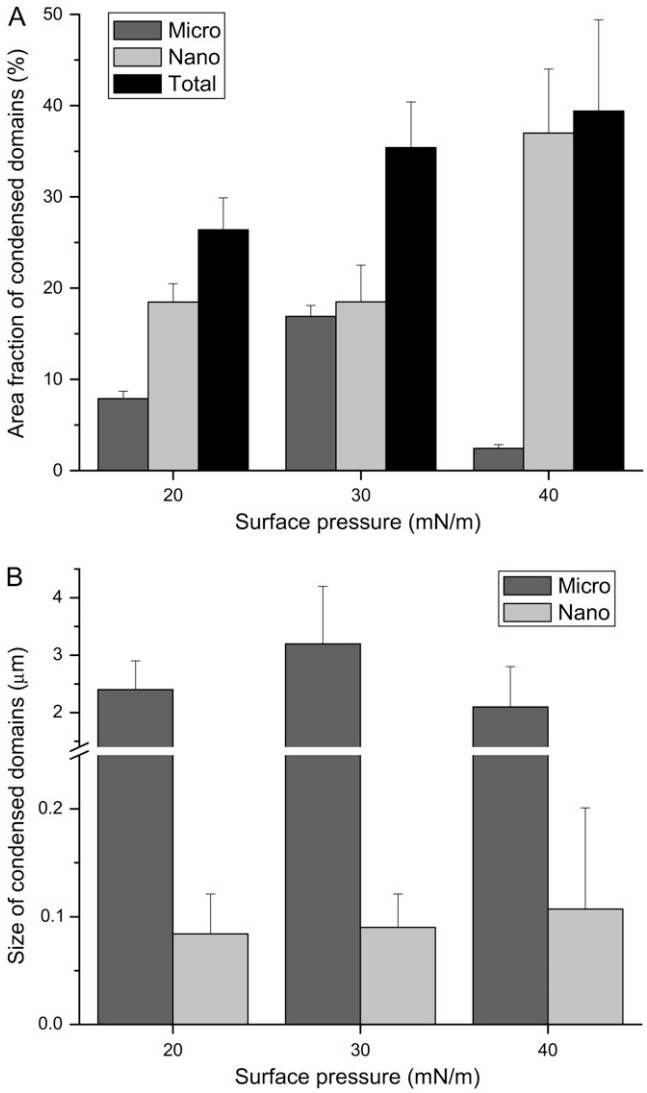

FIGURE 8 Quantification results of the development of microscale, nanoscale and total TC domains in BLES plus SP-A monolayers on compression. (*A*) Surface areas covered by the TC domains. (*B*) Size, i.e., equivalent diameter, of micro- and nanodomains. The quantification was conducted in the same way as for BLES films (Fig. 3).

40 mN/m. As shown in Fig. 9, considerably fewer networks of bright spots were found after chelation of calcium by EDTA. These are isolated patches with a maximum height of ~4 nm, which is close to the dimension of individual SP-A octadecamers, as shown previously by transmission electron microscopy (TEM) (49). All of this evidence suggests the bright spots detected by AFM are SP-A. Other features of these spots, such as their preferential concentration at the domain boundaries and the exclusion from the monolayer at 40 mN/m, also closely resemble the previously observed behavior of SP-A (50).

When π was increased to 50 mN/m (Fig. 6 *D*), the original monolayer was transformed to multilayers, as shown by a dramatic increase in height. These multilayers cover ~20% of the surface area. The height of these multilayers ranged from ~4 to ~28 nm (Figs. 6 *d* and 7 *d*), corresponding to ~1 to 7 stacks of PL bilayers. This is double the height of the multilayers generated in pure BLES films (Fig. 2 *d*), suggesting that SP-A promotes formation of bilayer stacks. It should be noted that it is difficult to differentiate PL multilayers and SP-A aggregates excluded from the interfacial monolayer purely based on the topographic analysis. However, two features would help to distinguish multilayers from SP-A aggregates: 1), the multilayers generally have a much larger diameter than SP-A aggregates; and 2), some multilayers clearly show stacked bilayers on top of each other (see the inset in Fig. 7 *D* for a surface plot of the layered multilayer structures). This feature is not applicable to SP-A aggregates.

DISCUSSION

Phase separation and transition in BLES films

Phase separation in BLES monolayers

Compression-driven PL phase separation in surfactant monolayers, indicated by domain formation and evolution, has been extensively studied previously by means of FM, BAM, and AFM. Most of these studies, however, were conducted with monolayers of single PL or ''model'' surfactants often consisting of simple mixtures of two or three PL components without or with only one hydrophobic surfactant protein, SP-B or SP-C, or analogs thereof. There are relatively few studies based on lipid extract surfactants containing the full complement of surfactant PL and SP-B plus SP-C. Discher et al. (14) studied the phase separation of monolayers of calf lung surfactant extract (CLSE) using FM and BAM. They found that at room temperature, phase separation, indicated by the formation of dye-excluding condensed domains, initiated at ~10 mN/m. On further compression, the area occupied by the condensed domains increased progressively and reached a maximum of 25 ± 5% at 35 mN/m. When π was further increased to 40 mN/m, the area of the condensed domains decreased dramatically to ~4%. Nag et al. (16) and Worthman et al. (51) found similar phase separation behavior in monolayers of a porcine lung surfactant extract (PLSE) using FM. During compression, the condensed PL domains started appearing at ~13 mN/m (16), increased to a maximum of 18% area at 25 mN/m, and decreased back to 3% at 40 mN/m (51). This AFM study of microscale TC domains in BLES monolayers (Fig. 3) is qualitatively and quantitatively consistent with these previous studies. Our previous study using ToF-SIMS has shown that the microscale TC domains in BLES consist mainly of DPPC and DPPG (24). The LE domains consist mainly of unsaturated PL and hydrophobic surfactant proteins (52).

In addition to the nucleation and evolution of microdomains, similar to those shown previously using FM and BAM, AFM shows new features, i.e., nanodomains embedded within the LE phase. These nanodomains have a size of

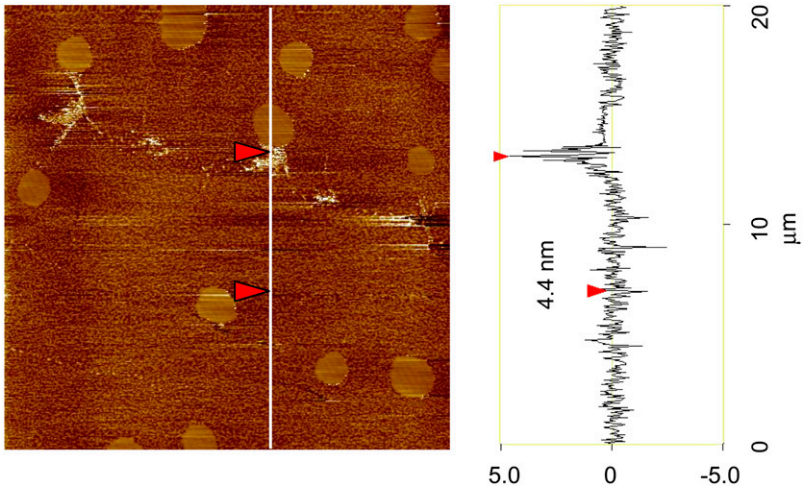

FIGURE 9 An AFM image of BLES with SP-A at 40 mN/m with the addition of 5 mM EDTA. The scan area is 20 × 20 μm. After chelation of calcium by EDTA, the PL domains are relatively unaffected. However, the network of bright spots is impaired. The maximum height of these spot is ~4 nm.

~60 nm and hence are below the resolution of optical imaging techniques (usually no smaller than 1 μm). The discovery of nanodomains with AFM has been reported previously in monolayers of stearic acid (37), DPPC (53–55), DPPC/DPPG (54), and BLES (25). For instance, Cruz et al. (54) found numerous nanometer sized TC domains in the LE phase of DPPC and DPPC/DPPG (7:3) monolayers. The topography and frictional properties of these nanodomains were found to be identical to the microscale TC domains, indicating similar molecular composition and arrangement in these domains despite the different size scales (54).

This work reports π-dependent nucleation and growth of nanodomains in BLES monolayers, as summarized in Fig. 3. In contrast to the microdomains, the area of the nanodomains increases monotonically with increasing π. The increase in nanodomains complements the decrease of microdomains and brings the total area covered by the TC phase up to 35–40% of the monolayer, approximately equal to the molecular fraction of DPPC plus other gel phase PL, such as DPPG, in BLES. This finding suggests that the nanodomains may develop at the cost of the microdomains. This argument is clearer in the case of SP-A-containing BLES monolayers. As summarized in Fig. 8, when π is increased from 30 to 40 mN/m, there is a significant decrease in microdomains and an increase in nanodomains. However, the total area of TC phase remains relatively unchanged.

The conversion from microdomains into nanodomains provides a logical explanation for the apparent ''remixing'' of TC and LE phases found previously by FM in PS monolayers at ~40 mN/m (14,16,51). At this π, the microscale TC domains dissociate into nanoscale domains that are uniformly ''dissolved'' into the LE phase. This TC–LE phase remixing results in a more homogeneous conformation than films consisting of fewer, much larger microdomains with the same area scattered in the LE phase. Such a film conformation may resemble a ''2D alloy'' (16,56), which imparts both stability and flexibility to the PS film, simultaneously.

Previous studies using different subfractions of CLSE suggested that phase remixing in surfactant monolayers requires cholesterol (57). Cholesterol partitions into the TC phase and helps decrease line tension to zero when the monolayers are compressed to the critical pressure required for remixing to occur (57–59). This study, however, suggests that the phase remixing may not necessarily require cholesterol as BLES is devoid of cholesterol (38). Our previous studies (25) have shown that adding a physiological amount of cholesterol (20 mol %) into BLES increased the number of microdomains and decreased their average size. However, the effect of cholesterol on nanodomains remains unclear.

Nevertheless the evolution of domains in BLES monolayers does conform to a line tension decrease during film compression. The equilibrium domain morphology (shape and size) of a PL monolayer is determined by the balance between line tension and long range dipole-dipole repulsion between lipid molecules (60,61). The line tension tends to minimize the domain boundaries by producing a small number of larger domains and by imposing a round shape on the individual domains. The dipolar repulsion works in the opposite way. The breakup of microdomains into nanodomains hence reflects a decrease in line tension. Also consistent with this view is the distortion of the shape of the microdomains found at 40 mN/m (Fig. 2 *C*).

Kinetically-dependent domain morphology

This study showed that PL phase separation, i.e., the formation of both microscale and nanoscale TC domains, can be obtained either by compression or by directly accumulating surfactant at the interface. A film spread to 30 mN/m (film spreading completed within 10 s) shows more but smaller microdomains than films compressed slowly to the same π (Fig. 4 *B* vs. Fig. 2 *B*). This domain morphology resembles films quickly compressed to the same π (Fig. 4 *C*). These experimental data may suggest: 1), the compression-driven

LE-to-TC phase transition also occurs in spread films, hence, it is not compression per se but the increase in lipid packing that causes the phase separation in PL monolayers; 2), spreading films to high π by directly accumulating surfactant at the interface may be equivalent to compressing the films at high rates; and 3), the microdomain morphology in PL monolayers at a certain π is determined by kinetic factors, e.g., the rate of film compression or formation.

As mentioned above, the equilibrium domain morphology depends on the competition between line tension and electrostatic repulsion between lipid molecules (60,61). However, a true equilibrium between different PL phases in a monolayer is usually established so slowly that the actual domain morphology is normally determined by kinetic factors (60–62). It has been established both experimentally (16,37,63) and theoretically (60–62) that domain morphology is affected by the rate of compression. A fast compression results in more and smaller domains than a slow compression. This is because a faster compression allows less time for the phase equilibrium to be established than a slower compression. In agreement with this view, it has been found that allowing a longer time for equilibrium gave rise to a rounder shape of the condensed domains and less heterogeneity inside these domains (55,57,63).

Monolayer-to-multilayer transition in BLES films

When π was increased from 40 to 50, the compression isotherms for BLES films exhibit a plateau at which the film compressibility is significantly higher than either before or after the plateau (Fig. 1). Similar plateaus have been observed in Langmuir films of model surfactants with hydrophobic surfactant proteins (SP-B and/or SP-C) (64,65), PL mixtures with a significant amount of fluid PL and/or neutral lipids (19,57), and lipid extract surfactants (16,51), including BLES (24,66). However, in single or in mixtures of disaturated PL, such as DPPC and DPPC/DPPG (52,65,67), such plateaus do not occur at room temperature.

AFM studies on model systems (such as DPPC/DPPG, 4:1 or DPPC/POPG/palmitic acid, 7:2:1) with SP-B (52,65) or SP-C (20,21) or short peptides of these proteins (3,22) have confirmed that the occurrence of such a plateau during compression corresponds to a transition from a monolayer to multilayers. Consequently, such plateaus have traditionally been called ''squeeze-out'' plateaus where a surfactant monolayer partially collapses to accommodate the increased surface pressure (68). However, it should be noted that the ''squeeze-out'' occurring during the monolayer-to-multilayer transition is intrinsically different from the classical ''squeeze-out'' model (11–13), as discussed in the Introduction. The classical squeeze-out model predicted that PS films maintain stability by selectively excluding non-DPPC components from the interfacial monolayers. However, ToF-SIMS studies have showed that the squeezed out multilayers contained not only hydrophobic proteins (69) but also DPPC (23). Hence, the multilayers would appear to show no significant differences from the interfacial monolayer in terms of composition.

This study has confirmed that the monolayer-to-multilayer transition occurs in BLES films during the squeeze-out plateau (Fig. 2). At 50 mN/m, the multilayers range from 4 to 12 nm high, accounting for ~1 to 3 stacks of PL bilayers. The resulting multilayer structures cover only ~15% of the surface area. However, taking into account their 3D architecture, these multilayers store a significant amount of excess surface active material, which may respread into the interfacial monolayer on film expansion. This has been confirmed in our study: when films were expanded from $\pi > 50$ mN/m back to 30 mN/m, both micro- and nanodomains appeared again (Fig. 4 *A*), although with a morphology somewhat different from that observed during the original compression. This difference in film morphology is consistent with the π–A hysteresis shown in the compression–expansion isotherm (Fig. 1). The hysteresis also prevents the study of film recompression using our small trough, in which LB transfer is limited to a minimum surface area of 15–20%. The reversibility of the monolayer-to-multilayer transition indicates that after squeeze-out the excluded multilayers remain closely associated with the interfacial monolayer rather than escaping into the aqueous subphase. On expansion, the excess PL stored in the multilayers readily returns back into the interface to decrease surface tension. Hence, the formation of multilayer structures is a vital requirement for a functional PL film in at least two respects: 1), it imparts the surfactant film additional stability, thus facilitating reaching low surface tensions on further compression; and 2), it stores PL for film replenishment on subsequent expansion.

The monolayer-to-multilayer transition, or the general mechanism of partial collapse of PL monolayers, seems to require TC–LE phase coexistence (70,71). This requirement highlights the importance of surfactant proteins and fluid PL in PS. As reviewed above, partial collapse of a surfactant monolayer, as indicated by the squeeze-out plateau in the compression isotherms, only occurs for films that contain hydrophobic surfactant proteins and/or fluid PL. ToF-SIMS studies showed that the multilayers originated from the former LE phase (protein-enriched) of the monolayer (69,72). Detailed microscopic and theoretical studies on monolayers of model surfactants suggested that the transition initiated at TC–LE domain boundaries (73,74). At the domain boundaries, the elastic and frictional properties of the monolayer change dramatically, thus readily flawing under pressure. If this is the case, the breakup of the microdomains into the nanodomains, found before the 2D–3D transition, would result in a more nearly optimal conformation as this generates more homogeneous and much longer domain boundaries. Therefore, the conversion from microdomains into nanodomains may enhance the homogeneity of the multilayer structures. This view is qualitatively consistent with the experimental observations of Crane and Hall (75) and Smith et al. (76). They found that monolayers of CLSE or a single-

component fluid PL (such as POPC) can be transformed to a metastable structure when the monolayers are compressed to a π higher than π_e using a sufficiently rapid compression in a captive bubble surfactometer (CBS). Such a rapid compression is expected to facilitate the formation of nanodomains, as shown in Fig. 4 *C*.

Another potential benefit that may arise from the formation of the multilayer structures is the so-called ''lotus effect'' (77). It has been found that nanoscale surface topography has a profound effect on the surface wettability (78,79). A surface roughness in the scale of several tens of nanometers was found to significantly enhance the hydrophobicity of the surface (78,79). Hence, the transition from monolayers into multilayers may result in a natural superhydrophobic surface, which renders additional water-repellency to the hydrophobic monolayer of PS. Such a superhydrophobic interfacial film in vivo would be more efficient in repelling water from the interface, thereby more efficiently reaching very low surface tensions.

Two different multilayer morphologies

A close scrutiny of the multilayer structures showed two different micromorphologies: isolated disk-like structures with uniform height and pyramidical structures where smaller protrusions were stacked on top of bigger ones (Fig. 2 *d*). The height of each layer of the protrusions is ~4–5 nm, indicating bilayer stacks (46). The former structures have been reported for a SP-B containing model surfactant (52). The latter structure was found in SP-C containing systems (20,21,69). Such a morphological difference between SP-B and SP-C promoted multilayers can be explained by their different molecular structures. SP-B may promote multilayer formation by rimming and buckling bilayer pockets adjacent to the interfacial monolayer (52,80). In contrast, SP-C may help stabilize the multilayer structures by spanning stacks of PL bilayers through its hydrophobic α-helix, i.e., by positioning a transmembrane orientation (20,21,69) while remaining associated with the monolayer by its N-terminal Cys-esterified palmitates. This SP-C model was supported by the direct measurement of helix orientation at the air–water interface using IR reflection–adsorption spectroscopy (IRRAS) (67). BLES contains both SP-B and SP-C, ~1:3 by weight (81). The identification of both multilayer morphologies in BLES may suggest that SP-B and SP-C promote the multilayer formation independently.

It should be noted that AFM cannot discern whether the multilayers are protruded toward the air or to the aqueous subphase, by simply analyzing film topography. Both recent molecular dynamics simulations (82) and direct AFM scan at the air–water interface (83) suggested that the multilayers were oriented toward the aqueous phase. If this is the case, the multilayer structure detected by AFM (Figs. 2 *D* and 7 *D*) would be ''upside-down'' compared to the structure at the air–water interface, i.e., with the protruded multilayers facing the mica surface and wrapped by the interfacial monolayer originally at the air–water interface (83). Although this would not affect the topographical analysis of the multilayer structure, it can introduce artifact to the morphological analysis of the multilayers. As a result, no firm conclusion on the multilayer morphology of BLES can be drawn from the current topographical analysis. Evidence along this line requires more investigation.

Effect of SP-A on surface activity and domain formation of BLES films

SP-A enhances adsorption but not dynamic surface activity

SP-A does not significantly vary the shape of compression isotherms of BLES monolayers and the location of the squeeze-out plateau (Fig. 5 vs. Fig. 1). In other words, SP-A has little effect on the dynamic surface activity of PS, i.e., those biophysical properties related to the attainment of low surface tensions. This is consistent with previous studies on PLSE (51) and CLSE (84). Consistent with these in vitro observations, SP-A knockout mice can breathe normally (85). These studies suggest that SP-A is not physiologically indispensable for the normal biophysical function of PS. More recent studies suggest that the main function of SP-A is in pulmonary host defense (86).

Nevertheless, the most striking effect of SP-A on the surface activity of BLES is in film formation. With the addition of a trace of SP-A (2.5 wt% of PL in BLES) half the amount of BLES spread at the interface can increase π to the same or even a higher level than BLES alone. This finding is consistent with previous in vitro studies using the pulsating bubble surfactometer (34) and CBS (35), and in vivo studies using fibrinogen-insulted rabbits (87). These studies suggested that SP-A improves the surface activity of lipid extract surfactants by enhancing the rate of adsorption. Such an effect was found to be dependent on SP-B and calcium (84,88).

SP-A promotes formation of nanodomains

This study found that SP-A does not significantly vary the nucleation and growth of microdomains in BLES monolayers (Fig. 6 vs. Fig. 2). In the presence of SP-A and calcium, the microdomains undergo a similar transition to that found in the absence of SP-A: they first increase the area fraction to a maximum at 30 mN/m and then decrease significantly at 40 mN/m (Fig. 8). This trend is consistent with previous studies of PLSE in the presence of SP-A using FM (51). In contrast, SP-A plays an important role in promoting nanodomains. At 20 mN/m, nanodomains already appear in SP-A-containing BLES monolayers, whereas they are absent without SP-A. This finding is consistent with a previous report that SP-A produced more, smaller condensed domains in DPPC monolayers at the same range of π as studied here (50). The presence of the nanodomains increases the total area of TC phase at 20 mN/m to ~25%, which is approximately fivefold the TC

phase observed at this π in the absence of SP-A. The case of low π (e.g., 20 mN/m), i.e., high surface tension, represents an early stage of adsorption. Hence, the increase in TC phase in the monolayer due to the SP-A-induced nanodomains is likely to be a consequence of the rapid adsorption promoted by SP-A, which increases the rate of lipid packing in the monolayer.

With SP-A, a significant number of nanodomains are formed immediately before the onset of monolayer-to-multilayer transition, i.e., at 40 mN/m. However, the total areas of the TC phase are relatively unchanged between 30 and 40 mN/m. These areas are also similar to BLES films without SP-A, and are approximately equal to the molar fraction of gel phase disaturated PL in BLES. As discussed above, the dissociation of microdomains into nanodomains significantly increases the length of TC–LE domain boundaries at which the monolayer-to-multilayer transition may initiate. Consequently, such a molecular conformation is expected to produce more and uniformly distributed nucleation sites for monolayer-to-multilayer transition when further increasing π.

SP-A facilitates the monolayer-to-multilayer transition

Schurch et al. (35) found that SP-A not only promoted adsorption of PS at low concentrations, but also decreased the area reduction required to reach low surface tensions and improved film stability at these low surface tensions. However, in contrast to this work, those studies were conducted for compression of adsorbed films in a CBS. Hence the enhancement in dynamic surface activity found in those studies is in a surface tension range lower than the equilibrium value and ought to be related to the surfactant reservoir attached to the interfacial monolayer. Schurch et al. (35,89) hypothesized that SP-A may enhance the dynamic surface activity by prompting the formation of the surfactant reservoir. This hypothesis has been supported by Yu and Possmayer (90) who showed that SP-A promoted formation of DPPC-containing bilayers below the air–water interface with adsorbed BLES films.

This study provides direct evidence indicating that SP-A promotes the formation of multilayers originating from a monolayer under compression. It is shown that the number of multilayers formed in the SP-A-containing BLES films is double that in the absence of SP-A (~7 vs. 3 PL bilayers). AFM shows SP-A is excluded from the BLES monolayer at 40 mN/m (Figs. 6 *C* and 7 *C*). Hence, the role of SP-A in the formation of multilayers at 50 mN/m can only be indirect. This study supports the view that SP-A may promote multilayer formation indirectly by producing more nanoscale TC domains before the 2D–3D transition. This effect of SP-A is hence analogous to the contribution of a rapid compression to PL monolayers without SP-A.

Physiological relevance of domain formation

Extrapolation of the domain morphology found in this study to the in vivo surfactant lining layer must be conducted with caution. The domain morphology and phase behavior of monolayers are dependent on multiple factors, including the molecular composition of the film, surface pressure, rate of film compression, subphase pH, temperature, and perhaps humidity and other environmental factors.

In contrast to BLES, endogenous surfactant contains cholesterol, which is known to play a profound role in varying the phase behavior of PL bilayers and monolayers (25,57,59,91,92). Further, temperature has a large influence on the phase behavior of PL monolayers (14). The surfactant film in vivo seems to be formed by rapid adsorption and hence would be always associated with a surfactant reservoir. Surface tension in the lungs during normal tidal breathing likely varies from a near-zero value to no more than 30 mN/m (i.e., π from ~40 to 70 mN/m) (7,93). The surface area of alveoli varies only slightly (94) but with a much faster rate than the compression rate used in a LWB.

Despite these deviations, this study provides a biophysical model of how PS might reach low surface tensions. A functional PS film may reach low surface tension by forming kinetically-controlled nanoscale TC domains. These nanodomains are distributed uniformly in the LE phase, thus forming a 2D alloy-type structure that imparts both flexibility and stability to the film. On further compression, such an alloy structure also facilitates partial collapse of surfactant monolayers from the domain boundaries. The resultant multilayer structures could provide additional stability to PS films, thereby allowing the attainment of very low surface tensions. SP-A promotes the formation of nanodomains by accelerating adsorption and increasing the rate of lipid packing. As a result, SP-A enhances the formation of multilayers and hence film stability at low surface tensions.

We thank Dr. Lijuan Yao for isolating SP-A and Mr. Robert Harbottle for helpful discussion. We thank BLES Biochemicals Inc. for the generous donation of BLES.

This work was supported by the Canadian Institutes of Health Research grant No. MOP-64406 (to N.P.) and grant No. FRN-15462 (to F.P.). YYZ is grateful to Natural Sciences and Engineering Research Council of Canada for Postdoctoral Fellowship 328777-2006.

REFERENCES

1. Possmayer, F. 2004. Physicochemical aspects of pulmonary surfactant. *In* Fetal and Neonatal Physiology. R. A. Polin, W. W. Fox, and S. H. Abman, editors. W. B. Saunders Company, Philadelphia. 1014–1034.
2. Rodriguez-Capote, K., K. Nag, S. Schurch, and F. Possmayer. 2001. Surfactant protein interactions with neutral and acidic phospholipid films. *Am. J. Physiol. Lung Cell. Mol. Physiol.* 281:L231–L242.
3. Takamoto, D. Y., M. M. Lipp, A. von Nahmen, K. Y. Lee, A. J. Waring, and J. A. Zasadzinski. 2001. Interaction of lung surfactant proteins with anionic phospholipids. *Biophys. J.* 81:153–169.
4. Biswas, S. C., S. B. Rananavare, and S. B. Hall. 2007. Differential effects of lysophosphatidylcholine on the adsorption of phospholipids to an air/water interface. *Biophys. J.* 92:493–501.
5. Seifert, M., D. Breitenstein, U. Klenz, M. C. Meyer, and H. J. Galla. 2007. Solubility versus electrostatics: what determines lipid/protein interaction in lung surfactant. *Biophys. J.* 93:1192–1203.

6. Zuo, Y. Y., and F. Possmayer. 2007. How does pulmonary surfactant reduce surface tension to very low values? *J. Appl. Physiol.* 102:1733–1734.
7. Schurch, S. 1982. Surface tension at low lung volumes: dependence on time and alveolar size. *Respir. Physiol.* 48:339–355.
8. Gaines, G. L. 1966. Insoluble Monolayers at Liquid-Gas Interfaces. InterScience Publishers, John Wiley & Sons, New York.
9. Veldhuizen, R., K. Nag, S. Orgeig, and F. Possmayer. 1998. The role of lipids in pulmonary surfactant. *Biochim. Biophys. Acta.* 1408:90–108.
10. Postle, A. D., E. L. Heeley, and D. C. Wilton. 2001. A comparison of the molecular species compositions of mammalian lung surfactant phospholipids. *Comp. Biochem. Physiol. A Mol. Integr. Physiol.* 129:65–73.
11. Watkins, J. C. 1968. The surface properties of pure phospholipids in relation to those of lung extracts. *Biochim. Biophys. Acta.* 152:293–306.
12. Clements, J. A. 1977. Functions of the alveolar lining. *Am. Rev. Respir. Dis.* 115:67–71.
13. Bangham, A. D., C. J. Morley, and M. C. Phillips. 1979. The physical properties of an effective lung surfactant. *Biochim. Biophys. Acta.* 573:552–556.
14. Discher, B. M., K. M. Maloney, W. R. Schief, Jr., D. W. Grainger, V. Vogel, and S. B. Hall. 1996. Lateral phase separation in interfacial films of pulmonary surfactant. *Biophys. J.* 71:2583–2590.
15. von Nahmen, A., A. Post, H.-J. Galla, and M. Sieber. 1997. The phase behavior of lipid monolayers containing pulmonary surfactant protein C studied by fluorescence light microscopy. *Eur. Biophys. J.* 26: 359–369.
16. Nag, K., J. Perez-Gil, M. L. Ruano, L. A. Worthman, J. Stewart, C. Casals, and K. M. Keough. 1998. Phase transitions in films of lung surfactant at the air-water interface. *Biophys. J.* 74:2983–2995.
17. Lipp, M. M., K. Y. Lee, A. Waring, and J. A. Zasadzinski. 1997. Fluorescence, polarized fluorescence, and Brewster angle microscopy of palmitic acid and lung surfactant protein B monolayers. *Biophys. J.* 72:2783–2804.
18. Discher, B. M., W. R. Schief, V. Vogel, and S. B. Hall. 1999. Phase separation in monolayers of pulmonary surfactant phospholipids at the air-water interface: composition and structure. *Biophys. J.* 77:2051–2061.
19. Piknova, B., W. R. Schief, V. Vogel, B. M. Discher, and S. B. Hall. 2001. Discrepancy between phase behavior of lung surfactant phospholipids and the classical model of surfactant function. *Biophys. J.* 81:2172–2180.
20. Amrein, M., A. von Nahmen, and M. Sieber. 1997. A scanning force- and fluorescence light microscopy study of the structure and function of a model pulmonary surfactant. *Eur. Biophys. J.* 26:349–357.
21. von Nahmen, A., M. Schenk, M. Sieber, and M. Amrein. 1997. The structure of a model pulmonary surfactant as revealed by scanning force microscopy. *Biophys. J.* 72:463–469.
22. Ding, J., D. Y. Takamoto, A. von Nahmen, M. M. Lipp, K. Y. Lee, A. J. Waring, and J. A. Zasadzinski. 2001. Effects of lung surfactant proteins, SP-B and SP-C, and palmitic acid on monolayer stability. *Biophys. J.* 80:2262–2272.
23. Bourdos, N., F. Kollmer, A. Benninghoven, M. Ross, M. Sieber, and H. J. Galla. 2000. Analysis of lung surfactant model systems with time-of-flight secondary ion mass spectrometry. *Biophys. J.* 79:357–369.
24. Harbottle, R. R., K. Nag, N. S. McIntyre, F. Possmayer, and N. O. Petersen. 2003. Molecular organization revealed by time-of-flight secondary ion mass spectrometry of a clinically used extracted pulmonary surfactant. *Langmuir.* 19:3698–3704.
25. Keating, E., L. Rahman, J. Francis, A. Petersen, F. Possmayer, R. Veldhuizen, and N. O. Petersen. 2007. Effect of cholesterol on the biophysical and physiological properties of a clinical pulmonary surfactant. *Biophys. J.* 93:1391–1401.
26. Grunder, R., P. Gehr, H. Bachofen, S. Schurch, and H. Siegenthaler. 1999. Structures of surfactant films: a scanning force microscopy study. *Eur. Respir. J.* 14:1290–1296.
27. Kaganer, V. M., H. Mohwald, and P. K. Dutta. 1999. Structure and phase transitions in Langmuir monolayers. *Rev. Mod. Phys.* 71:779–819.
28. Possmayer, F., K. Nag, K. Rodriguez, R. Qanbar, and S. Schurch. 2001. Surface activity in vitro: role of surfactant proteins. *Comp. Biochem. Physiol. A Mol. Integr. Physiol.* 129:209–220.
29. McCormack, F. X. 1998. Structure, processing and properties of surfactant protein A. *Biochim. Biophys. Acta.* 1408:109–131.
30. Voss, T., H. Eistetter, K. P. Schafer, and J. Engel. 1988. Macromolecular organization of natural and recombinant lung surfactant protein SP 28–36. Structural homology with the complement factor C1q. *J. Mol. Biol.* 201:219–227.
31. Casals, C. 2001. Role of surfactant protein A (SP-A)/lipid interactions for SP-A functions in the lung. *Pediatr. Pathol. Mol. Med.* 20: 249–268.
32. Williams, M. C., S. Hawgood, and R. L. Hamilton. 1991. Changes in lipid structure produced by surfactant proteins SP-A, SP-B, and SP-C. *Am. J. Respir. Cell Mol. Biol.* 5:41–50.
33. Veldhuizen, R. A., L.-J. Yao, S. A. Hearn, F. Possmayer, and J. F. Lewis. 1996. Surfactant-associated protein A is important for maintaining surfactant large-aggregate forms during surface-area cycling. *Biochem. J.* 313:835–840.
34. Chung, J., S. H. Yu, J. A. Whitsett, P. G. Harding, and F. Possmayer. 1989. Effect of surfactant-associated protein-A (SP-A) on the activity of lipid extract surfactant. *Biochim. Biophys. Acta.* 1002:348–358.
35. Schurch, S., F. Possmayer, S. Cheng, and A. M. Cockshutt. 1992. Pulmonary SP-A enhances adsorption and appears to induce surface sorting of lipid extract surfactant. *Am. J. Physiol.* 263:L210–L218.
36. Connell, S. D., and D. A. Smith. 2006. The atomic force microscope as a tool for studying phase separation in lipid membranes. *Mol. Membr. Biol.* 23:17–28.
37. Chi, L. F., M. Anders, H. Fuchs, R. R. Johnston, and H. Ringsdorf. 1993. Domain structures in Langmuir-Blodgett films investigated by atomic force microscopy. *Science.* 259:213–216.
38. Yu, S., P. G. Harding, N. Smith, and F. Possmayer. 1983. Bovine pulmonary surfactant: chemical composition and physical properties. *Lipids.* 18:522–529.
39. Yu, S. H., W. Chung, R. W. Olafson, P. G. Harding, and F. Possmayer. 1987. Characterization of the small hydrophobic proteins associated with pulmonary surfactant. *Biochim. Biophys. Acta.* 921:437–448.
40. Rodriguez-Capote, K., F. X. McCormack, and F. Possmayer. 2003. Pulmonary surfactant protein-A (SP-A) restores the surface properties of surfactant after oxidation by a mechanism that requires the Cys6 interchain disulfide bond and the phospholipid binding domain. *J. Biol. Chem.* 278:20461–20474.
41. Bligh, E. G., and W. J. Dyer. 1959. A rapid method of total lipid extraction and purification. *Can. J. Biochem. Physiol.* 37:911–917.
42. Haagsman, H. P., R. T. White, J. Schilling, K. Lau, B. J. Benson, J. Golden, S. Hawgood, and J. A. Clements. 1989. Studies of the structure of lung surfactant protein SP-A. *Am. J. Physiol.* 257:L421–L429.
43. Bailey, T. C., A. A. Maruscak, A. Petersen, S. White, J. F. Lewis, and R. A. Veldhuizen. 2006. Physiological effects of oxidized exogenous surfactant in vivo: effects of high tidal volume and surfactant protein A. *Am. J. Physiol. Lung Cell. Mol. Physiol.* 291:L703–L709.
44. Lowry, O. H., N. J. Rosebrough, A. L. Farr, and R. J. Randall. 1951. Protein measurement with the Folin reagent. *J. Biol. Chem.* 193:265–275.
45. Zasadzinski, J. A., R. Viswanathan, L. Madsen, J. Garnaes, and D. K. Schwartz. 1994. Langmuir-Blodgett films. *Science.* 263:1726–1733.
46. Marsh, D. 1990. CRC Handbook of Lipid Bilayers. CRC Press, Boca Raton, FL.
47. Piknova, B., V. Schram, and S. B. Hall. 2002. Pulmonary surfactant: phase behavior and function. *Curr. Opin. Struct. Biol.* 12:487–494.
48. Ruano, M. L., I. Garcia-Verdugo, E. Miguel, J. Perez-Gil, and C. Casals. 2000. Self-aggregation of surfactant protein A. *Biochemistry.* 39:6529–6537.

49. Palaniyar, N., R. A. Ridsdale, F. Possmayer, and G. Harauz. 1998. Surfactant protein A (SP-A) forms a novel supraquaternary structure in the form of fibers. *Biochem. Biophys. Res. Commun.* 250:131–136.
50. Ruano, M. L., K. Nag, L. A. Worthman, C. Casals, J. Perez-Gil, and K. M. Keough. 1998. Differential partitioning of pulmonary surfactant protein SP-A into regions of monolayers of dipalmitoylphosphatidylcholine and dipalmitoylphosphatidylcholine/dipalmitoylphosphatidylglycerol. *Biophys. J.* 74:1101–1109.
51. Worthman, L. A., K. Nag, N. Rich, M. L. Ruano, C. Casals, J. Perez-Gil, and K. M. Keough. 2000. Pulmonary surfactant protein A interacts with gel-like regions in monolayers of pulmonary surfactant lipid extract. *Biophys. J.* 79:2657–2666.
52. Krol, S., M. Ross, M. Sieber, S. Kunneke, H. J. Galla, and A. Janshoff. 2000. Formation of three-dimensional protein-lipid aggregates in monolayer films induced by surfactant protein B. *Biophys. J.* 79: 904–918.
53. Hollars, C. W., and R. C. Dunn. 1998. Submicron structures in I-alpha dipalmitoylphosphatidylcholine monolayers and bilayers probed with confocal, atomic force and near field microscopy. *Biophys. J.* 75:342–353.
54. Cruz, A., L. Vazquez, M. Velez, and J. Perez-Gil. 2004. Effect of pulmonary surfactant protein SP-B on the micro- and nanostructure of phospholipid films. *Biophys. J.* 86:308–320.
55. Cruz, A., L. Vazquez, M. Velez, and J. Perez-Gil. 2005. Influence of a fluorescent probe on the nanostructure of phospholipid membranes: dipalmitoylphosphatidylcholine interfacial monolayers. *Langmuir.* 21: 5349–5355.
56. Perez-Gil, J. 2002. Molecular interactions in pulmonary surfactant films. *Biol. Neonate.* 81(Suppl 1):6–15.
57. Discher, B. M., K. M. Maloney, D. W. Grainger, C. A. Sousa, and S. B. Hall. 1999. Neutral lipids induce critical behavior in interfacial monolayers of pulmonary surfactant. *Biochemistry.* 38:374–383.
58. Benvegnu, D. J., and H. M. McConnell. 1992. Line tension between liquid domains in lipid monolayers. *J. Phys. Chem.* 96:6820–6824.
59. Discher, B. M., K. M. Maloney, D. W. Grainger, and S. B. Hall. 2002. Effect of neutral lipids on coexisting phases in monolayers of pulmonary surfactant. *Biophys. Chem.* 101–102:333–345.
60. McConnell, H. M., and V. T. Moy. 1988. Shapes of finite two-dimensional lipid domains. *J. Phys. Chem.* 92:4520–4525.
61. McConnell, H. M. 1991. Structures and transitions in lipid monolayers at the air-water interface. *Annu. Rev. Phys. Chem.* 42:171–195.
62. McConnell, H. M. 1996. Equilibration rates in lipid monolayers. *Proc. Natl. Acad. Sci. USA.* 93:15001–15003.
63. Klopfer, K. J., and T. K. Vanderlick. 1996. Isotherms of dipalmitoylphosphatidylcholine (DPPC) monolayers: Features revealed and features obscured. *J. Colloid Interface Sci.* 182:220–229.
64. Taneva, S., and K. M. Keough. 1994. Pulmonary surfactant proteins SP-B and SP-C in spread monolayers at the air-water interface: III. Proteins SP-B plus SP-C with phospholipids in spread monolayers. *Biophys. J.* 66:1158–1166.
65. Diemel, R. V., M. M. Snel, A. J. Waring, F. J. Walther, L. M. van Golde, G. Putz, H. P. Haagsman, and J. J. Batenburg. 2002. Multilayer formation upon compression of surfactant monolayers depends on protein concentration as well as lipid composition. An atomic force microscopy study. *J. Biol. Chem.* 277:21179–21188.
66. Nag, K., J. S. Pao, R. R. Harbottle, F. Possmayer, N. O. Petersen, and L. A. Bagatolli. 2002. Segregation of saturated chain lipids in pulmonary surfactant films and bilayers. *Biophys. J.* 82:2041–2051.
67. Wang, L., P. Cai, H. J. Galla, H. He, C. R. Flach, and R. Mendelsohn. 2005. Monolayer-multilayer transitions in a lung surfactant model: IR reflection-absorption spectroscopy and atomic force microscopy. *Eur. Biophys. J.* 34:243–254.
68. Keough, K. M. W. 1992. Physical chemistry of pulmonary surfactant in the terminal air spaces. *In* Pulmonary Surfactant: From Molecular Biology to Clinical Practice. B. Robertson, L. M. G. Van Golde, and J. J. Batenburg, editors. Elsevier, Amsterdam. 109–164.
69. Galla, H. J., N. Bourdos, A. Von Nahmen, M. Amrein, and M. Sieber. 1998. The role of pulmonary surfactant protein C during the breathing cycle. *Thin Solid Films.* 327–329:632–635.
70. Lipp, M. M., K. Y. Lee, J. A. Zasadzinski, and A. J. Waring. 1996. Phase and morphology changes in lipid monolayers induced by SP-B protein and its amino-terminal peptide. *Science.* 273:1196–1199.
71. Zasadzinski, J. A., J. Ding, H. E. Warriner, F. Bringezu, and A. J. Waring. 2001. The physics and physiology of lung surfactants. *Curr. Opin. Colloid Interface Sci.* 6:506–513.
72. Kramer, A., A. Wintergalen, M. Sieber, H. J. Galla, M. Amrein, and R. Guckenberger. 2000. Distribution of the surfactant-associated protein C within a lung surfactant model film investigated by near-field optical microscopy. *Biophys. J.* 78:458–465.
73. Diamant, H., T. A. Witten, A. Gopal, and K. Y. C. Lee. 2000. Unstable topography of biphasic surfactant monolayers. *Europhys. Lett.* 52: 171–177.
74. Diamant, H., T. A. Witten, C. Ege, A. Gopal, and K. Y. C. Lee. 2001. Topography and instability of monolayers near domain boundaries. *Phys. Rev. E Stat. Nonlin. Soft Matter Phys.* 63:061602.
75. Crane, J. M., and S. B. Hall. 2001. Rapid compression transforms interfacial monolayers of pulmonary surfactant. *Biophys. J.* 80:1863–1872.
76. Smith, E. C., J. M. Crane, T. G. Laderas, and S. B. Hall. 2003. Metastability of a supercompressed fluid monolayer. *Biophys. J.* 85:3048–3057.
77. Marmur, A. 2004. The Lotus effect: superhydrophobicity and metastability. *Langmuir.* 20:3517–3519.
78. Lau, K. K. S., J. Bico, K. B. K. Teo, M. Chhowalla, G. A. J. Amaratunga, W. I. Milne, G. H. McKinley, and K. K. Gleason. 2003. Superhydrophobic carbon nanotube forests. *Nano Lett.* 3: 1701–1705.
79. Lee, W., M. K. Jin, W. C. Yoo, and J. K. Lee. 2004. Nanostructuring of a polymeric substrate with well-defined nanometer-scale topography and tailored surface wettability. *Langmuir.* 20:7665–7669.
80. Lipp, M. M., K. Y. C. Lee, D. Y. Takamoto, J. A. Zasadzinski, and A. J. Waring. 1998. Coexistence of buckled and flat monolayers. *Phys. Rev. Lett.* 81:1650–1653.
81. Yu, S. H., and F. Possmayer. 1988. Comparative studies on the biophysical activities of the low-molecular-weight hydrophobic proteins purified from bovine pulmonary surfactant. *Biochim. Biophys. Acta.* 961:337–350.
82. Baoukina, S., L. Monticelli, M. Amrein, and D. P. Tieleman. 2007. The molecular mechanism of monolayer-bilayer transformations of lung surfactant from molecular dynamics simulations. *Biophys. J.* 93:3775–3782.
83. Knebel, D., M. Sieber, R. Reichelt, H. J. Galla, and M. Amrein. 2002. Scanning force microscopy at the air-water interface of an air bubble coated with pulmonary surfactant. *Biophys. J.* 82:474–480.
84. Venkitaraman, A. R., S. B. Hall, J. A. Whitsett, and R. H. Notter. 1990. Enhancement of biophysical activity of lung surfactant extracts and phospholipid-apoprotein mixtures by surfactant protein A. *Chem. Phys. Lipids.* 56:185–194.
85. Korfhagen, T. R., M. D. Bruno, G. F. Ross, K. M. Huelsman, M. Ikegami, A. H. Jobe, S. E. Wert, B. R. Stripp, R. E. Morris, S. W. Glasser, C. J. Bachurski, H. S. Iwamoto, and J. A. Whitsett. 1996. Altered surfactant function and structure in SP-A gene targeted mice. *Proc. Natl. Acad. Sci. USA.* 93:9594–9599.
86. Crouch, E., and J. R. Wright. 2001. Surfactant proteins A and D and pulmonary host defense. *Annu. Rev. Physiol.* 63:521–554.
87. Sun, B., T. Curstedt, G. Lindgren, B. Franzen, A. A. Alaiya, A. Calkovska, and B. Robertson. 1997. Biophysical and physiological properties of a modified porcine surfactant enriched with surfactant protein A. *Eur. Respir. J.* 10:1967–1974.
88. Yu, S. H., and F. Possmayer. 1994. Effect of pulmonary surfactant protein A (SP-A) and calcium on the adsorption of cholesterol and film stability. *Biochim. Biophys. Acta.* 1211:350–358.

89. Schurch, S., R. Qanbar, H. Bachofen, and F. Possmayer. 1995. The surface-associated surfactant reservoir in the alveolar lining. *Biol. Neonate*. 67:61–76.

90. Yu, S. H., and F. Possmayer. 1996. Effect of pulmonary surfactant protein A and neutral lipid on accretion and organization of dipalmitoylphosphatidylcholine in surface films. *J. Lipid Res.* 37:1278–1288.

91. Bernardino de la Serna, J., J. Perez-Gil, A. C. Simonsen, and L. A. Bagatolli. 2004. Cholesterol rules: direct observation of the coexistence of two fluid phases in native pulmonary surfactant membranes at physiological temperatures. *J. Biol. Chem.* 279:40715–40722.

92. Leonenko, Z., S. Gill, S. Baoukina, L. Monticelli, J. Doehner, L. Gunasekara, F. Felderer, M. Rodenstein, L. M. Eng, and M. Amrein. 2007. An elevated level of cholesterol impairs self-assembly of pulmonary surfactant into a functional film. *Biophys. J.* 93:674–683.

93. Schurch, S., J. Goerke, and J. A. Clements. 1978. Direct determination of volume- and time-dependence of alveolar surface tension in excised lungs. *Proc. Natl. Acad. Sci. USA*. 75:3417–3421.

94. Bachofen, H., and S. Schurch. 2001. Alveolar surface forces and lung architecture. *Comp. Biochem. Physiol. A Mol. Integr. Physiol.* 129: 183–193.